EDGE ARTICLE

Check for updates

All publication charges for this article have been paid for by the Royal Society of Chemistry

Controlling triplet-pair formation in acene-bridged trimers through locally excited–charge-transfer state mixing†

Ebin Sebastian, [a] Daniel G. Congrave, ‡[bc] Jeroen Royakkers, ‡[b] Stephanie Montanaro,[b] Huaxi Huang,[d] Ashish Sharma,[a] Julia Osmólska,[a] He Zhu,[b] Chanakarn Phansa,[a] Jurjen Winkel,[a] Oliver Millington,[b] Murad J. Y. Tayebjee,[e] Luis M. Campos,[d] Hugo Bronstein *[ab] and Akshay Rao *[a]

Singlet fission (SF) offers a pathway to surpass conventional efficiency limits in photovoltaics, yet how bridge–chromophore coupling governs locally excited/charge-transfer state (LE–CT) mixing and thereby the multiexciton yield remains elusive. We design three systems, **TIPS-BT0**, **TIPS-TAT**, and **Encap-TAT**, that progressively increase bridge–chromophore coupling. Steady-state spectroscopy and transient absorption reveal that **TIPS-BT0** and **TIPS-TAT** undergo efficient SF, forming correlated triplet pairs (^{1}TT) and, in **TIPS-TAT**, long-lived triplets. By contrast, **Encap-TAT** loses vibronic structure and relaxes ultrafast into a broad, red-shifted intramolecular exciplex-like (Ex) state. Quantum chemical analysis shows that the Ex state originates from strong hybridization between local excitations (LEs) and bridge–chromophore CT configurations, driven by large electron and hole transfer integrals and a small LE–CT energy gap. Such strong LE–CT hybridisation suppresses well-defined ^{1}TT formation, favouring intramolecular Ex emission and enhancing photoluminescence quantum yield ($\simeq$80.5% *vs.* $\simeq$38.5% for **TIPS-TAT**). These findings establish a unifying framework in which the balance between multiexciton generation and exciplex emission in acene-bridged trimers is governed by the degree of LE–CT mixing. Tuning bridge energetics and LE–CT offsets enables deliberate routing of excited-state pathways toward efficient triplet production or bright exciplex emission, providing actionable design rules for next-generation singlet-fission and optoelectronic architectures.

Introduction

Singlet fission (SF) is a spin-conserving multiexciton generation process in which one singlet exciton (S_1) splits into two triplet excitons (T_1), potentially doubling the exciton yield per absorbed photon and enabling photovoltaics to transcend the Shockley–Queisser limit.[1–5] Although crystalline acenes and their derivatives first showcased intermolecular SF, their limited exciton diffusion, aggregation, and heterogeneous packing hinder practical device integration.[6–8] In contrast, covalent intramolecular SF (iSF) molecules and polymers have

[a]*Cavendish Laboratory, University of Cambridge, Cambridge, CB3 0HE, UK. E-mail: ar525@cam.ac.uk; hab60@cam.ac.uk*

[b]*Yusuf Hamied Department of Chemistry, University of Cambridge, Cambridge, CB2 1EW, UK*

[c]*Chemistry Research Labloratory, University of Oxford, Oxford, OX1 3TA, UK*

[d]*Department of Chemistry, Columbia University, New York, New York 10027, USA*

[e]*School of Photovoltaic and Renewable Energy Engineering, UNSW Sydney, Sydney, 2052, NSW, Australia*

† Chanakarn Phansa could not be contacted to confirm the final author list prior to acceptance.

‡ These authors contributed equally.

emerged as a powerful alternative, offering precise control over geometry, solution processability, and electronic coupling between chromophores (Fig. 1a).[9–18]

A central challenge in iSF design lies in balancing electronic interactions. The chromophores must couple strongly enough to form a correlated triplet pair (^{1}TT), yet remain sufficiently decoupled to allow triplet separation and avoid losses to excimer or charge-transfer (CT) traps.[19–23] π-Conjugated bridges are therefore widely employed, not only to enforce distance and connectivity[12,20,24–28] but also to actively tune the electronic landscape through resonance with chromophore frontier orbitals.[29–31] Strategies spanning phenylene spacers, extended acenes, and macrocyclic frameworks have been explored to tailor molecular geometry, connectivity, and coupling (Fig. 1a).[13,32–39] In particular, rigid macrocyclic/cyclophane platforms enable precise cofacial arrangements that tune electronic coupling, resulting in singlet fission with strongly geometry-dependent rates and, in some cases, long-lived multiexciton signatures.[40–43]

From a singlet-fission perspective, however, the role of CT-mediated interactions is nuanced. Moderate exciton–CT hybridisation can be advantageous, lowering the barrier to
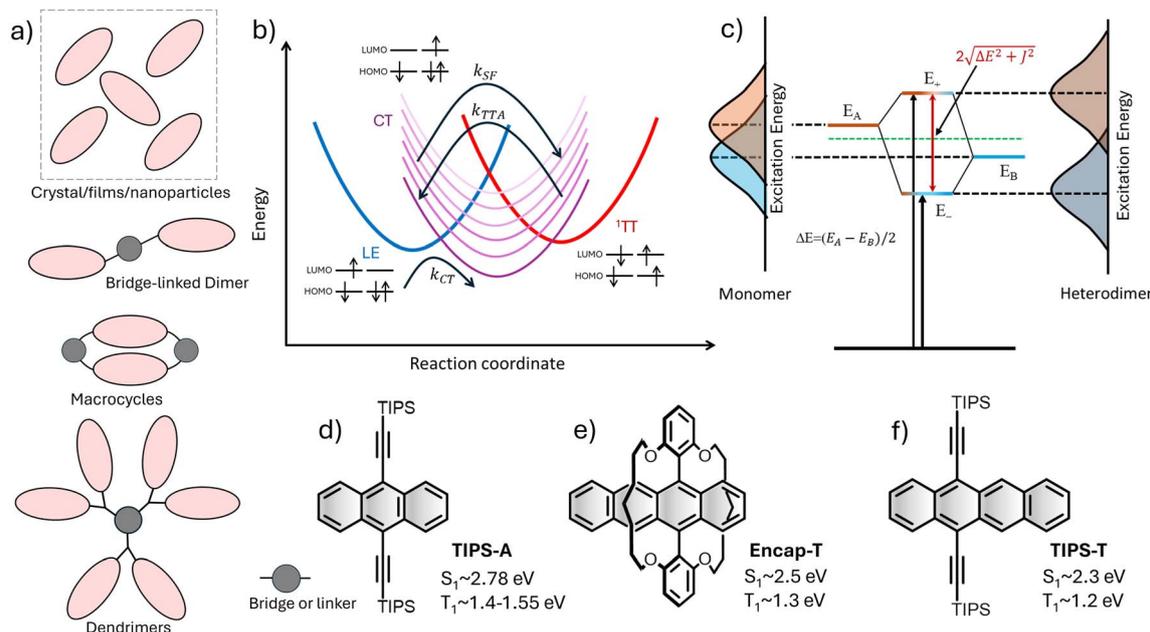
Fig. 1 (a) Molecular design strategies employed to achieve both intermolecular and intramolecular singlet fission, highlighting the transition from crystalline packing motifs to covalently bound multichromophoric scaffolds. (b) Schematic illustration showing intramolecular singlet fission with a charge-transfer (CT) state. The bright local exciton LE (blue) is coupled to a ladder of CT states (violet tones) whose relative energy shifts with solvent polarity, and to the correlated triplet pair (^{1}TT) (red). When the CT level is strongly stabilized, it behaves as a population trap (rate k_{CT}); when it remains off-resonant, it serves as a virtual superexchange mediator, enhancing LE → ^{1}TT conversion (rate k_{SF}). The same channel can also assist triplet–triplet annihilation back toward singlet character (rate k_{TTA}). (c) Energy level diagram depicting exciton coupling between two distinct chromophores (A and B), where mixing leads to the formation of new hybrid excitonic states (E_+ and E_-), separated by an energy splitting proporional to $\frac{E_A + E_B}{2} \pm \sqrt{\frac{\Delta E^2}{4} + J^2}$; here, ΔE is the energy mismatch, and J is the electronic coupling. (d, e and f) Chemical structures of the SF chromophores and bridges used in this study, along with their estimated singlet and triplet energies (S_1 and T_1, respectively), establish the energetic prerequisites for efficient intramolecular singlet fission.

accessing CT-mediated ^{1}TT configurations and facilitating spin–space decoherence required for triplet separation (Fig. 1b).[26,34–36,44–46] Yet excessive CT admixture can destabilize the ^{1}TT channel, funneling population into excimer-like manifolds that suppress free-triplet yield.[47–50] Particularly intriguing are cases where CT states localized on the bridge–chromophore axis hybridize with the local excitation of the fission-active unit. Such mixing may open superexchange pathways into ^{1}TT, or, if too strong, collapse the exciton into a delocalized LE–CT hybrid that bypasses multiexciton formation. Despite extensive efforts to tune electronic coupling through bridge design, the impact of bridge–chromophore resonance on LE–CT mixing and its consequences for singlet fission is not fully understood.

To address this gap, we employ a trimeric chromophore–bridge–chromophore scaffold as a minimal platform to tune LE–CT mixing while preserving a well-defined intramolecular SF motif on the terminal tetracenes. Relative to directly linked dimers, the bridge provides an independent handle over CT energetics and transfer integrals.[35,51] It can also modulate the triplet–triplet exchange interaction that governs whether ^{1}TT remains bound or separates into long-lived triplets. TIPS-anthracene (**TIPS-A**) was chosen as the bridge because its higher triplet energy avoids acting as a triplet sink or hetero-fission channel, while its conjugated framework enables

systematic control of electronic communication and CT-mediated superexchange. We further introduce Encap-tetracene (**Encap-T**) to reduce LE–CT detuning and increase bridge–chromophore resonance while preventing aggregation and improving solubility.[52] Accordingly, **TIPS-TAT** features a large CT–LE offset ($E_{CT} \approx 3.05$ eV; $E_{LE} \approx 2.30$ eV; $\Delta E_{CT–LE} = 0.75$) and weak LE–CT mixing, whereas **Encap-TAT** has a smaller gap ($E_{CT} \approx 2.85$ eV; $E_{LE} \approx 2.50$ eV; $\Delta E_{CT–LE} = 0.35$ eV) and stronger hybridisation. By mapping their optical signatures and fission dynamics, we show how increasing bridge resonance can either support long-lived triplets *via* CT-assisted superexchange or suppress iSF through exciplex-like trapping.

Results and discussion

Molecular synthesis and structures

To investigate how bridge–chromophore CT state alignment modulates the intramolecular singlet fission (iSF) landscape, we compared two trimeric scaffolds, **TIPS-TAT** and **Encap-TAT** (Fig. 2). Both architectures incorporate a TIPS-anthracene (**TIPS-A**) bridge; however, in **Encap-TAT** the local excited-state energy of the bridge is more closely aligned with that of the Encap-tetracene (**Encap-T**) chromophores. In addition, the charge-transfer (CT) state in **Encap-TAT** lies energetically closer to the
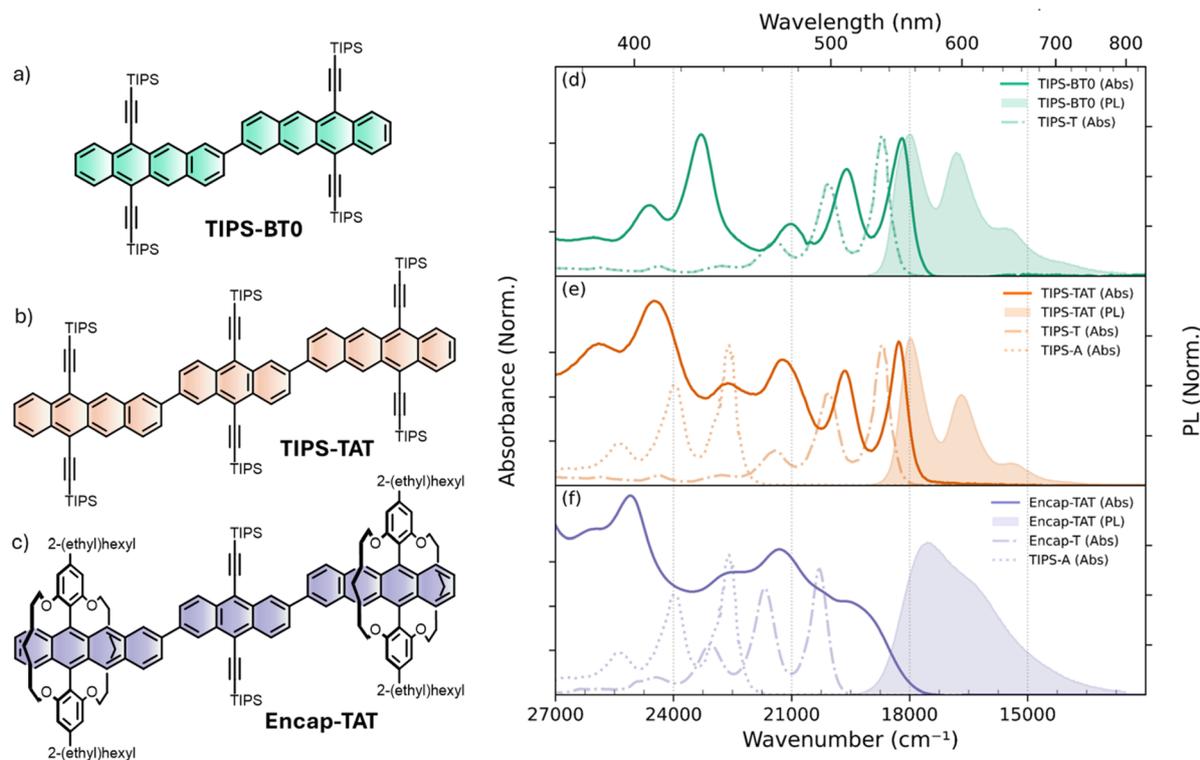
Fig. 2 Chemical structures (left) of the dimer **TIPS-BT0** (a), the trimer **TIPS-TAT** (b), and the encapsulated trimer **Encap-TAT** (c). Panels (d–f) show normalized absorption and photoluminescence (PL) spectra (right) of the chromophoric architectures in comparison with their corresponding monomeric subunits. All absorption (solid lines) and PL (filled curves) spectra are recorded in dilute toluene solution (~20 μM) at room temperature. The vibronic structure of **TIPS-T** is retained in **TIPS-BT0** and **TIPS-TAT**, while the pronounced spectral reshaping in **Encap-TAT** reflects strong electronic communication mediated through the central TIPS–A bridge. TIPS: triisopropylsilyl group.

local exciton (LE) state compared to **TIPS-TAT**, thereby enhancing the possibility of LE–CT hybridization. The synthesis of the dimer **TIPS-BT0** (Fig. 2a) and the trimer **TIPS-TAT** (Fig. 2b) has been reported previously.[51,53] Unlike the trimeric systems, **TIPS-BT0** is a directly linked TIPS-tetracene dimer without a bridging unit and thus serves as a baseline reference for iSF. Building on these precedents, **Encap-TAT** (Fig. 2c) was prepared *via* a convergent route culminating in a Suzuki cross-coupling onto a rigid macrocyclic scaffold (Schemes S1–S3). The macrocycle was deliberately chosen to suppress aggregation and finely tune the energetic alignment between bridge and chromophore units.[52] 2-(Ethyl)hexyl alkyl chains ensure sufficient solubility.

Across all three molecular architectures, from the dimer **TIPS-BT0** to the trimers **TIPS-TAT** and **Encap-TAT**, DFT calculations suggest that the dihedral angle (θ) between each tetracene unit and adjacent arene units is consistently ~32–33° (Fig. S1). This intrinsic twist and bulky solubilizing substituents suppress face-to-face π–π stacking while retaining orbital overlap sufficient for electronic communication (Fig. S2–S4). By combining structural rigidity with controlled connectivity, these scaffolds establish a well-defined platform for probing how bridge-mediated electronic alignment governs intramolecular singlet fission efficiency.

Steady-state optical characteristics and bridge–chromophore excitonic interaction. Fig. 2 shows the normalized absorption (solid lines) and photoluminescence (PL, filled

areas) spectra of the **TIPS-BT0**, **TIPS-TAT** and **Encap-TAT** trimer in dilute toluene ($c \approx 20$ μM). In the weak-to-intermediate coupling regime, where the electronic coupling J is small compared to the principal acene vibrational quantum ($\hbar\omega \approx 1400$ cm^{-1}), vibronic intensity ratios provide a more sensitive measure of excitonic delocalization than simple band shifts. In particular, the 0–0/0–1 ratio directly reflects exciton delocalization within a perturbative Franck–Condon excitation framework.[54–56]

The **TIPS-BT0** dimer (Fig. 2a, d and Table S1) exhibits the canonical TIPS-tetracene vibronic progression, with a sharp 0–0 band near 550 nm (18 182 cm^{-1}) and a 0–1 shoulder at ~510 nm (19 608 cm^{-1}). Compared to the monomer, enhanced 0–1 intensity signals weak H-type excitonic coupling between the tetracene units. In addition, a modest red shift of the excitonic band (~500 cm^{-1}) and the emergence of a CT-derived absorption feature near 429 nm (23 310 cm^{-1}), which borrows oscillator strength through LE–CT mixing is observed.[57] This reveals the presence of LE–CT interactions mediated by frontier orbital overlap between the chromophores.[58–60] The PL spectrum retains a well-resolved vibronic progression with a small Stokes shift (~196 cm^{-1}), confirming localized S$_1$ → S$_0$ emission.

Building on this reference case, incorporation of a **TIPS-A** bridge in the **TIPS-TAT** trimer introduces new spectral features (Fig. 2e). The asymmetric architecture relaxes symmetry

restrictions present in homodimers, allowing both the lower-energy ($S_0 \rightarrow S_1$) and higher-energy ($S_0 \rightarrow S_2$) transitions (Tables S2–S3 and Fig. 1C).[57] The $S_0 \rightarrow S_1$ transition ($\sim$547 nm, 18 282 cm^{-1}) retains the tetracene vibronic progression but shows enhanced 0–1 intensity, consistent with weak H-type excitonic coupling mediated through the bridge and exhibits a modest red shift ($\sim$400 cm^{-1}) relative to the **TIPS-T** monomer. A distinct ($S_0 \rightarrow S_2$) band at 471 nm (21 230 cm^{-1}) is red-shifted by $\sim$471 cm^{-1} relative to isolated **TIPS-A**, while a CT-derived band emerges near 408 nm with enhanced oscillator strength from LE–CT coupling.[57] Together, these signatures confirm appreciable orbital overlap across the trimer backbone and modest LE–CT mixing. The PL spectrum preserves the tetracene-like vibronic structure, indicating that despite through-bridge interactions, emission remains dominated by localized **TIPS-T** excitons.

By contrast, **Encap-TAT** (Fig. 2c, f and S5) displays qualitatively different optical behavior. Fusing **Encap-T** units that are more closely aligned in energy with the **TIPS-A** bridge erases monomeric vibronic progression, yielding a broad, vibronically unresolved absorption envelope (27 000–21,000 cm^{-1}). The PL spectrum is likewise broad, red-shifted, featureless with a large Stokes shift ($\sim$1932 cm^{-1}). These trends are consistent with a substantially reduced LE–CT separation in **Encap-TAT** ($\Delta E_{CT-LE} \approx 0.35$) relative to **TIPS-TAT** (≈ 0.75 eV), which enhances LE–CT hybridisation and favors relaxation into an intramolecular exciplex-like minimum.[56,61] Overall, the progression from **TIPS-TAT** to **Encap-TAT** shows that decreasing LE–CT separation drives increasingly strong hybridization, with **Encap-TAT**'s PL consistent with intramolecular excimer/exciplex-like emission.

Single-arm Encap-TA: isolating bridge-mediated interactions. To probe the origin of **Encap-TAT**'s distinctive optical response, we synthesized the single-arm **Encap-TA** dimer (Scheme S3) and performed steady-state optical measurements to quantify bridge–chromophore interactions (Fig. 3). As shown in Fig. 3c, the normalized absorption (solid) and PL (dashed) spectra of **Encap-T** (monomer, black), **Encap-TA** (dimer, red), and **Encap-TAT** (trimer, blue) reveal a clear progression from a localized chromophore to an intermediate, single-arm dimer, and finally to a strongly LE–CT coupled trimer.

In contrast to the broadened, featureless absorption of **Encap-TAT**, **Encap-TA** displays a structured spectrum with well-resolved vibronic features. Two lower-energy peaks at $\sim$512 nm (19 531 cm^{-1}) and $\sim$479 nm (20 878 cm^{-1}), assigned to the $S_0 \rightarrow S_1$ progression (Table S4) are weaker than a higher-energy band at $\sim$453 nm (22 076 cm^{-1}). This inversion of intensity reflects contributions from both S_1 and S_2 transitions and is consistent with an intermediate-coupling regime, moderate H-type excitonic coupling, together with differences in transition-dipole strengths for the **Encap-T** chromophore and the **TIPS-A** bridge (Fig. S6 and Table S2). A modest red shift in both LE derived (Frenkel-type) bands, peak broadening, and the appearance of a CT feature near $\sim$385 nm (25 974 cm^{-1}) further indicate LE–
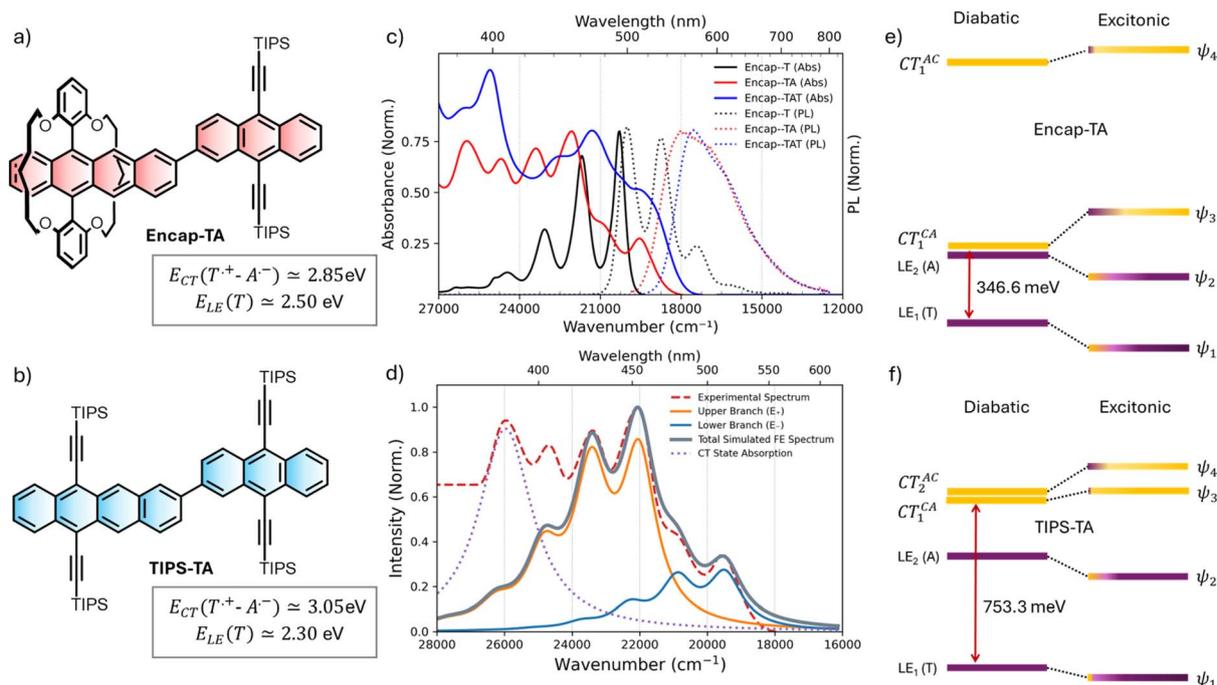

Fig. 3 Molecular structure of the **Encap-TA** dimer (a), composed of an **Encap-T** chromophore covalently linked to a TIPS-A bridge and **TIPS-TA** dimer (b), featuring a direct connection between **TIPS-T** and TIPS-A units. (c) Normalized absorption (solid lines) and photoluminescence (PL) spectra (dotted lines) of the monomeric unit (**Encap-T**), dimer (**Encap-TA**), and trimer **Encap-TAT**, recorded in dilute toluene ($c \approx 20$ μM). (d) Experimental absorption spectrum of **Encap-TA** (gray) fitted using an exciton-vibrational coupling model, resolving contributions from the upper (E_+) and lower (E_-) excitonic branches, a CT-like state, and vibronically structured LE components. Schematic energy-level diagrams showing diabatic electronic states (LE and CT, before mixing) and the resulting adiabatic excitonic states (after mixing) for **Encap-TA** (e) and **TIPS-TA** (f). The adiabatic eigenstates (ψ_1–ψ_4) are significant mixtures of the underlying diabatic LE and CT states.

CT coupling (in the diabatic basis) that yields LE–CT mixing and appreciable bridge–chromophore electronic communication.[61,62] Notably, relative to **Encap-TA**, the **Encap-TAT** trimer exhibits additional red shifts of the $S_0 \rightarrow S_1/S_2$ envelope and the CT band, signalling much stronger LE–CT hybridisation in the trimer.

While the **Encap-TA** absorption remains vibronically resolved, its PL collapses into a broad, featureless envelope that is markedly broader and more red-shifted than the monomer (Fig. 3c). The monomer's 0–0 fluorescence at ~500 nm (20 012 cm^{-1}) is only ~7 nm (~270 cm^{-1}) red-shifted from its 0–0 absorption, whereas the **Encap-TA** PL peaks at ~555 nm (~18 018 cm^{-1}), exhibiting a ~43 nm (~1513 cm^{-1}) Stokes shift and loss of vibronic structure. These pronounced red shifts and broadened, structureless PL in both **Encap-TA** and **Encap-TAT** are consistent with emission from a relaxed excited-state minimum that lies below the initially prepared Franck–Condon bright state. This behaviour is characteristic of an intramolecular exciplex-like (CT-stabilised) emissive state, i.e., emission from an adiabatic surface with enhanced CT character upon structural/solvent relaxation.[47,63–66]

The experimental absorption spectrum of the heterodimer **Encap-TA** was quantitatively reproduced by a full vibronic Frenkel-exciton model (Fig. 3f and see Section 1.12 in the SI), which decomposes the response into lower (E_-) and upper (E_+) excitonic branches. The best fit was obtained using a transition-dipole ratio of $\mu_2/\mu_1 = 0.75$ and $J = 334$ cm^{-1}. In a heterodimer, the loss of inversion symmetry "lights up" both excitons, so E_- and E_+ each carry oscillator strength (Fig. 1c). By contrast, a symmetric homodimer supports one bright and one dark exciton (Fig. S7).[61,67–69] In our fit, E_- captures the red-shifted S_1 manifold (Table S2), while E_+ accounts for the enhanced exciton-like (LE-derived) higher-energy feature near ~480 nm. The charge-transfer (CT) contribution is modelled as a single Lorentzian centered at ~26 000 cm^{-1} (~385 nm), shown as the purple dotted trace in Fig. 3d (Section 1.12, SI).

Quantifying LE–CT mixing in Encap-TA and TIPS-TA. To validate our spectroscopic assignments, we quantified LE–CT mixing in the **Encap-TA** and **TIPS-TA** dimers by constructing and diagonalising a four-state diabatic Hamiltonian in the localized configuration basis $\{|\text{LE}_A\rangle, |\text{LE}_B\rangle, |\text{CT}_{CA}\rangle, |\text{CT}_{AC}\rangle\}$, where $|CA)\rangle \equiv A^{\cdot+}–B^{\cdot-}$ and $|AC\rangle \equiv A^{\cdot-}–B^{\cdot+}$ (Section 1.8–1.11, SI). Diagonalization results in four adiabatic states (ψ_1–ψ_4)

whose LE-subspace (excitonic) vs. CT-subspace weights, obtained from the eigenvector coefficients, are reported in Table 1 and correlated with the spectra in Fig. 3e and f. In this Hamiltonian, LE–CT coupling is mediated by the electron- and hole-transfer integrals (t_e, t_h). In both dimers, t_e and t_h exceed the LE–LE coulombic coupling (J_{Coul}), indicating that charge-mediated superexchange coupling rather than direct coulomb coupling governs interunit communication (Tables S5–S8). LE–CT mixing refers exclusively to the LE vs. CT composition of these adiabatic eigenstates (ψ_1–ψ_4).

For the **Encap-TA** dimer, the two lowest adiabatic states are LE-dominant but carry substantial CT content (ψ_1, $\psi_2 \approx$ 83–81% LE/17–19% CT; Tables 1 and S9). Both are stabilized relative to their diabatic LE site energies (−804.0 cm^{-1} for ψ_1) and (−663.9 cm^{-1} for ψ_2), consistent with strong CT-mediated mixing and the red-shifted LE envelope (Fig. 3e). Concomitantly, a nominal CT state (ψ_3) is mixed down and acquires appreciable LE character (~31%), evidencing pronounced LE–CT hybridization. In parallel, level repulsion destabilizes the diabatic CT manifold by several hundred cm^{-1} leaving the CT states high in energy yet optically active via LE–CT mixing. Despite the CT adiabats lying several thousand cm^{-1} above the LE manifold, this superexchange is sufficient to (i) stabilize the bright LE pair (spectral red shift), (ii) activate CT-derived absorption via oscillator-strength borrowing, and (iii) broaden/soften vibronic structure mirroring the observed absorption and PL trends of **Encap-TA** (and, amplified further, in **Encap-TAT**).

In contrast, **TIPS-TA** displayed weaker LE and CT mixing. ψ_1 remains highly localized (~95% LE) and ψ_2 shows only modest CT admixture (~17% CT), while the upper pair is largely CT-like (ψ_3–$\psi_4 \gtrsim$ 81–97% CT; Tables 1 and S10). Spectroscopically, optical features of the **TIPS-TAT** dimer are consistent with the electronic structure derived from the **TIPS-TA** model, comprising two stabilized LE-derived (exciton-like) absorption bands with only modest CT admixture, a weak intensity-borrowed CT band, and comparatively narrower vibronic signatures (Fig. 3f). The difference relative to **Encap-TA** arises from smaller effective LE–CT coupling and a larger LE–CT energy separation, which together suppress hybridization into the lowest bright states. Taken together, these results highlight starkly different mixing regimes. **Encap-TA** exhibits strong CT-mediated superexchange that injects appreciable CT character into the lowest LE-derived (exciton-like) adiabatic state, while **TIPS-TA** supports a more localized lowest state with only minor CT admixture.

Impact of LE–CT hybridisation on intramolecular singlet fission

In this section, we investigate how strong excitonic hybridization between local exciton (LE) states and bridge– chromophore charge-transfer (CT) states reshape the excited-state manifold and perturb the kinetic landscape of intramolecular singlet fission. To probe these effects, we performed both femtosecond and nanosecond transient absorption (fs/nsTA) measurements

Table 1 Energies and local-excitation (LE) vs. charge-transfer (CT) composition of the adiabatic excited states formed upon diagonalization of a 4-state diabatic Hamiltonian. ψ_1–ψ_4 denote eigenstates in ascending energy

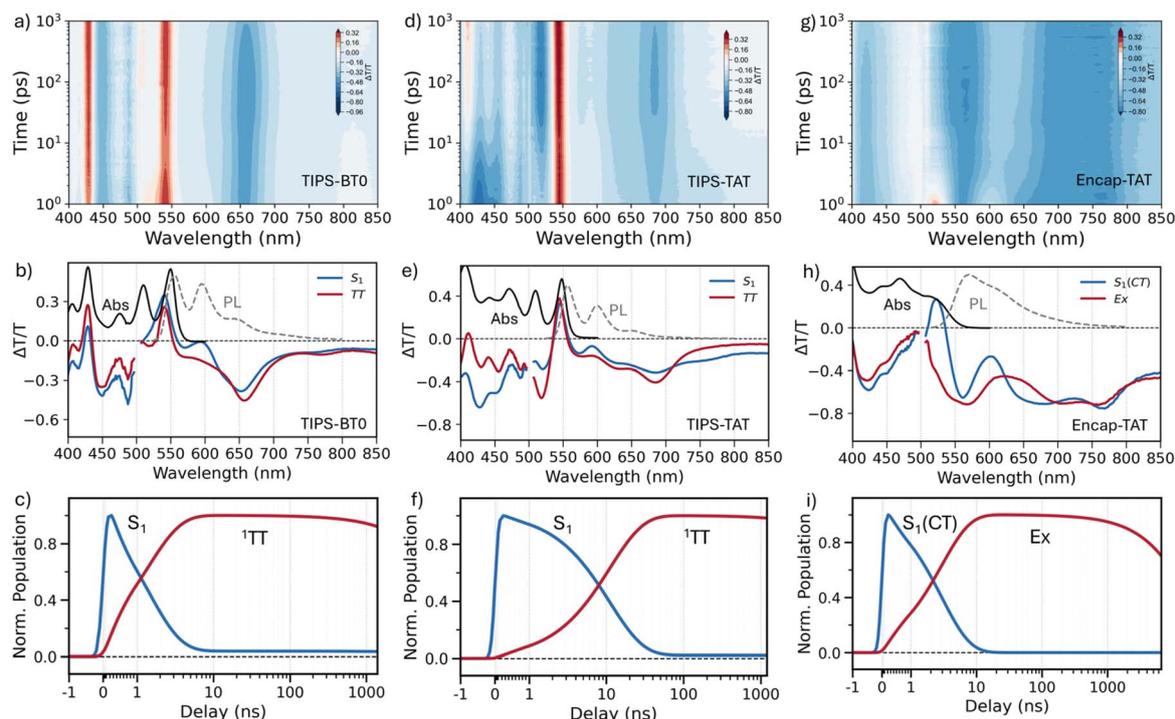| State	TIPS-TA			Encap-TA		
	Energy (cm^{-1})	LE (%)	CT (%)	Energy (cm^{-1})	LE (%)	CT (%)
ψ_1	18 226.95	95.3	4.7	19 359.78	83.3	16.7
ψ_2	21 742.32	82.8	17.2	21 745.28	81.4	18.6
ψ_3	24 848.05	2.9	97.1	24 056.15	31.1	68.9
ψ_4	25 609.39	19.0	81.0	29 849.95	4.3	95.7

Fig. 4 Femtosecond transient absorption (fsTA) spectra of **TIPS-BT0** (a), **TIPS-TAT** (d), and **Encap-TAT** (g) in toluene following 530 nm excitation, showing the evolution of the excited-state features as a function of delay time. Species-associated spectra (SAS) obtained from target analysis are shown for **TIPS-BT0** (b) and **TIPS-TAT** (e) while evolution-associated difference spectra (EADS) obtained from global analysis are shown for **Encap-TAT** (h). The corresponding time-dependent species populations from the target/global analysis are shown in (c), (f), and (i) for **TIPS-BT0**, **TIPS-TAT**, and **Encap-TAT**, respectively.

on **TIPS-BT0**, **TIPS-TAT**, and **Encap-TAT** in toluene ($c \approx 100~\mu M$) at room temperature. Fig. 4a, d and g shows the fsTA contour maps ($\Delta T/T$ as a function of probe wavelength and pump-probe delay) for the three systems following photoexcitation at 530 nm. Target/global analysis of the fsTA datasets using the kinetic schemes described in Section 1.7 in the SI yields the evolution- and species-associated spectra summarized in Fig. 4.[70,71]

Upon photoexcitation, **TIPS-BT0** (Fig. 4a–c) exhibits the characteristic $S_1 \rightarrow S_n$ photoinduced absorption (PIA) bands of **TIPS-T** or tetracene dimer chromophores centered at $\simeq 657$ nm and $\simeq 446$ nm, accompanied by ground-state bleach (GSB) features near $\simeq 541$ nm and $\simeq 430$ nm.[48,72–74] Target analysis reveals that the initially populated S_1 state decays with a lifetime of 1.39 ± 0.03 ps, concomitant with the rise of a correlated triplet pair (^1TT) PIA, centred at 520 nm, spanning the 570–615 nm region as well as 657 nm. The ^1TT population persists beyond the temporal window of the fsTA measurement. In the nanosecond transient absorption (nsTA) data (Fig. 5a, instrument response $\simeq 1$–2 ns), the same ^1TT-associated PIA features are observed at early times. These then decay mono-exponentially with a lifetime of $\tau_{TT} \simeq 8.7 \pm 0.4$ ns, ultimately leaving only a weak residual signal assigned to long-lived triplet (T_1) state PIA (Fig. S8–S10). The absence of correlated triplet pair dissociation into free triplets ($^1TT \rightarrow 2T_1$) is attributed to strong electronic communication between the chromophores and a high triplet–triplet exchange interaction. This elevated

exchange coupling stabilizes the bound ^1TT state and suppresses spin decoherence, thereby preventing its evolution into two non-interacting triplet excitons.[75,76]

The fsTA response of the **TIPS-TAT** trimer shows qualitatively similar characteristic S_1 state features, with $S_1 \rightarrow S_n$ PIA spanning from ~ 590 nm to 850 nm, a GSB centred around ~ 544 nm and prominent PIA bands below ~ 475 nm region (Fig. 4d–f and S11). While the singlet-state features resemble those of the monomer, the increased spectral broadening may arise from modest CT admixture/exciton–CT hybridisation in the initially accessed adiabatic manifold. Additionally, introducing a **TIPS-A** bridge that is closely aligned in energy substantially alters the ensuing excited-state kinetics. The rise of the ^1TT precursor in **TIPS-TAT**, tracked by PIA bands at 517 nm and 572–702 nm, occurs with $\tau_{SF} \simeq 11.2 \pm 0.06$ ps, in line with the previous reports,[28,51] but significantly slower than the 1.39 ps observed for **TIPS-BT0**. This deceleration reflects the longer centre-to-centre separation and added torsional flexibility introduced by the anthracene linker. Once formed, the ^1TT state in **TIPS-TAT** is remarkably long-lived ($\tau_{TT} \simeq 127.56 \pm 1$ ns), $\sim 15\times$ longer than in the directly linked dimer and it undergoes partial separation of the correlated pair ($^1TT \rightarrow 2T_1$) to yield free triplets (Fig. 5b, d and S12).

Quantitatively, from the fitted reversible $S_1 \rightleftharpoons {}^1TT$ kinetics, we estimate correlated triplet-pair yields of $\phi_{TT} = 96.97\%$ (**TIPS-BT0**) and 98.02% (**TIPS-TAT**). Using the triplet-plateau analysis (SI Section 1.13), the yields of persistent isolated triplets are
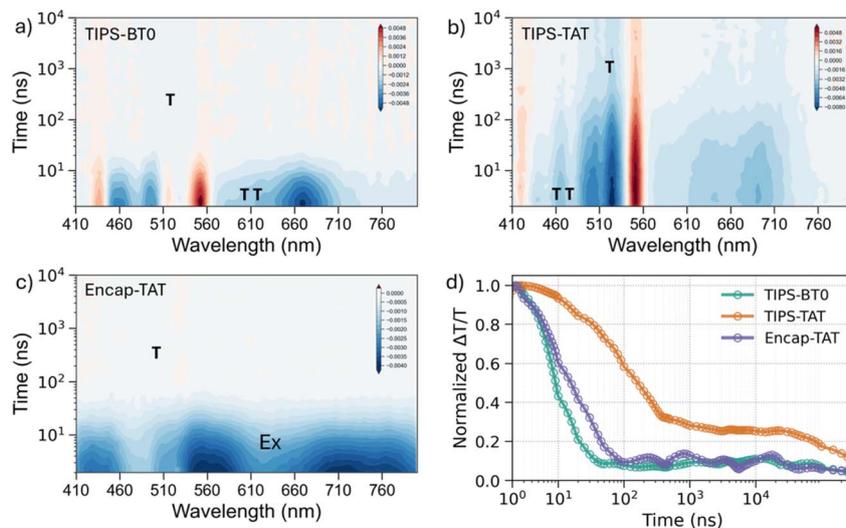
Fig. 5 Nanosecond transient absorption (nsTA) data of **TIPS-BT0** (a), **TIPS-TAT** (b), and **Encap-TAT** (c) in toluene following 532 nm photoexcitation, highlighting the spectral signatures of free triplets (T), correlated triplet pair (^{1}TT), and intramolecular exciplex state (Ex). (d) Corresponding kinetic traces monitored at the respective triplet PIA maxima: **TIPS-BT0** (480–510 nm), **TIPS-TAT** (500–520 nm), and **Encap-TAT** (470–500 nm), illustrating differences in triplet decay dynamics across the series.

~15.5% (**TIPS-BT0**) and ~58.8% (**TIPS-TAT**). Thus, while ^{1}TT formation is near-quantitative in both **TIPS-BT0** and **TIPS-TAT**, triplet separation is markedly more efficient in **TIPS-TAT**, underscoring the sensitivity of free-triplet generation to bridge-controlled exciton–CT mixing. This pronounced stabilization of the ^{1}TT manifold highlights how bridge-resonant coupling can both extend multiexciton lifetimes and boost free-triplet yields, even while moderating the initial fission rate. In the case of **TIPS-TAT**, the presence of the bridge reduces the triplet–triplet exchange interaction between the terminal **TIPS-T** units, thereby facilitating spin decoherence and promoting the formation of spatially separated, long-lived free triplets.

In stark contrast, **Encap-TAT** exhibits a fundamentally different early-time TA signature. Upon 530 nm excitation, its $S_1 \rightarrow S_n$ photoinduced absorption (PIA) no longer displays well-resolved peaks characteristic of the monomer **Encap-T** (Fig. 4g–i and S13–S15). Instead, it emerges as a broad, red-shifted, structureless band spanning ≃550–850 nm, with the ground-state bleach confined to ≲525 nm. This simultaneously red-shifted, unstructured PIA is consistent with substantial CT admixture in the lowest adiabatic manifold, as quantified for **Encap-TA** (≈17–19% CT) and expected to be enhanced in **Encap-TAT** given the smaller LE–CT detuning and stronger bridge–chromophore coupling. We therefore assign this feature to a singlet exciton with significant CT admixture, hereafter denoted as S_1 (CT). The initially populated S_1 (CT) feature decays with $\tau_{Ex} \simeq 2.95 \pm 0.04$ ps into a second state whose PIA is broader and completely unstructured across the probe window. The decay of the initially populated state is markedly faster than in **TIPS-TAT**, and the resulting spectral profile closely resembles the intramolecular excimer-like states reported in related chromophoric systems.[48,63–66,77,78] This is markedly different from the well-defined ^{1}TT signature seen in **TIPS-BT0** or **TIPS-TAT** and similar tetracene derivatives.[7,73]

We therefore refer to this broad, unstructured transient state as an intramolecular exciplex-like state (Ex) under dilute conditions. Here, Ex denotes a relaxed minimum on an exciton–CT-hybrid adiabatic surface with substantial bridge–chromophore CT character. We attribute Ex formation to structural and solvent relaxation on this hybrid surface, which progressively stabilises a more CT-rich minimum along the nuclear coordinate. Such relaxation can access a distribution of closely spaced relaxed minima (exciplex-like conformers) on the excited-state landscape, consistent with the progressive broadening and loss of vibronic structure observed in the transient absorption.[47,64] The Ex-state decays with a lifetime of ≃ 16.9 ± 0.2 ns back to the ground state, leaving only a very weak residual PIA attributable to long-lived T_1 excitons (Fig. S16 and Table S11). The assignment of this exciplex-like state, as a CT-stabilised relaxed minimum on an exciton–CT hybrid surface, is further supported by solvent-dependent steady-state photo-physics. In **Encap-TAT**, the PL maximum exhibits a pronounced red shift with increasing solvent polarity, whereas **TIPS-TAT** shows no such solvatochromic response (Fig. S17). Polarity stabilises CT states and enhances LE–CT mixing, whereas higher concentrations can introduce intermolecular excimer/aggregation pathways. Accordingly, measurements were performed under dilute conditions ($c \approx 100$ μM) to minimise intermolecular contributions, and solvent-dependent TA data are provided in the SI (Section 4, Fig. S18–S25) to support the CT-rich character of the Ex state. These solvent-dependent fsTA and nsTA measurements (SI Section 4, Fig. S18–S25) show that increasing polarity accelerates Ex formation and shortens its lifetime for **Encap-TAT**. In contrast, for the SF-active **TIPS-TAT**, increasing polarity primarily accelerates ^{1}TT formation without inducing comparable long-time quenching.

To further clarify the nature of this second component, we directly compared **Encap-TAT** with its single-arm analogue,
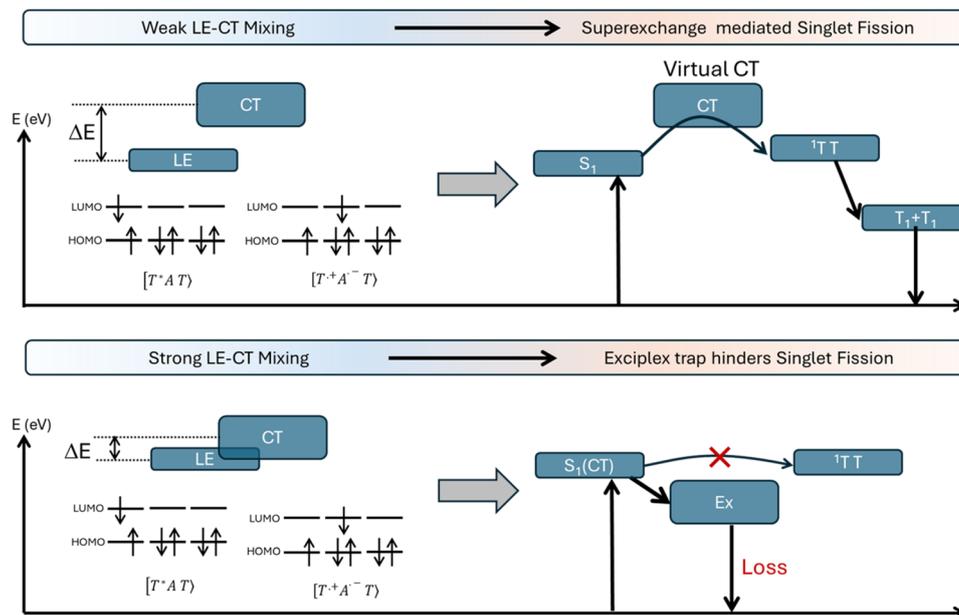
Fig. 6 LE–CT mixing governs whether singlet fission proceeds by superexchange or is quenched by an exciplex trap. The schematic summarizes two limiting regimes controlled by the LE–CT detuning and coupling. Top (weak LE–CT mixing; superexchange-mediated singlet fission): when the LE state of the terminal SF chromophore is energetically well separated from the CT configuration ($A^{\bullet-}$–$T^{\bullet+}$) CT remains largely virtual and mediates population transfer from S_1 to the correlated triplet pair ^{1}TT, followed by formation of separated triplets ($T_1 + T_1$). Bottom (strong LE–CT mixing; exciplex trap): when the LE and CT states are closer in energy and strongly coupled, substantial LE–CT hybridization yields a CT-enriched singlet S_1(CT) that relaxes to an intramolecular exciplex-like minimum (Ex). This trap diverts population away from S_1(CT) to ^{1}TT (red cross) and increases the non-productive loss. Thus, by tuning the LE–CT energy gap and state mixing, triplet-pair formation can be controlled.

Encap-TA (Fig. S26–30). In **Encap-TA**, the initially populated S_1(CT) state decays in $\simeq 2.25 \pm 0.06$ ps into an equally broad, featureless PIA band spanning the entire probe window, virtually identical in spectral shape and kinetics to the second component seen in **Encap-TAT**. This broad PIA then relaxes to the ground state with a long-lived residual ($\tau_2 \simeq$ 16–18 ns), consistent with a small population of free T_1 formed by inter-system crossing. Crucially, the close correspondence between **Encap-TA** and **Encap-TAT** excludes a conventional multiexciton (^{1}TT) assignment, since the triplet of **TIPS-A** lies far too high in energy to sustain a bound triplet pair with **Encap-T**.

Instead, we ascribe both decay components to a strongly mixed LE–CT hybrid state, hereafter denoted as the intra-molecular exciplex-like (Ex) state. This state arises from nuclear and structural relaxation in the excited state, aided by stabilization of the CT energy and significant electron- and hole-transfer integrals coupling the bridge and chromophores. These factors hybridise the local excitons with CT configurations into a continuous, unstructured excited-state manifold.[56,79–82] Importantly, such strong LE–CT hybridization suppresses the formation of well-defined triplet pairs localized on the terminal **Encap-T** units. The Ex-state instead forms on ultrafast timescales, outcompeting correlated triplet-pair formation, while simultaneously enhancing radiative decay pathways. This is consistent with the higher photoluminescence quantum yield observed for **Encap-TAT** (80.5%) compared to **TIPS-TAT** (~38.5%).

To rationalize the contrasting excited-state pathways, we summarize the role of LE–CT hybridization using the mechanistic schematic in Fig. 6. Under weak LE–CT mixing (top), exemplified by **TIPS-TAT**, the CT configuration associated with the bridge–chromophore pair remains largely virtual and mediates population transfer from S_1 to the correlated triplet pair ^{1}TT *via* a CT-assisted superexchange pathway, followed by formation of separated triplets ($T_1 + T_1$). In contrast, under strong LE–CT mixing (bottom), exemplified by **Encap-TAT**, reduced LE–CT detuning and enhanced coupling yield a CT-enriched singlet S_1(CT) that relaxes into an intramolecular exciplex-like minimum (Ex). This trap diverts population away from ^{1}TT formation and increases non-productive loss, consistent with the broadened, red-shifted spectral signatures and pronounced solvatochromic PL red shift observed for **Encap-TAT**.

Conclusions

By constructing the **TIPS-BT0** → **TIPS-TAT** → **Encap-TAT** series and combining steady-state/ultrafast spectroscopy with a four-state LE/CT diabatic Hamiltonian analysis, we show that bridge–chromophore energetic alignment governs exciton–CT hybridisation in the adiabatic excited states and thereby dictates the photophysical outcome in intramolecular singlet fission (iSF). In **TIPS-TAT**, a larger LE–CT energy offset limits the CT admixture while retaining sufficient LE ↔ CT coupling to enable CT-assisted superexchange into ^{1}TT, yielding long-lived, separable triplets. Although both **TIPS-BT0** and **TIPS-TAT** exhibit near-quantitative correlated triplet-pair formation ($\phi_{TT} >$ 95%), the isolated triplet yield differs substantially (~16% for

TIPS-BT0 *vs.* ~59% for **TIPS-TAT**), demonstrating that triplet separation is highly sensitive to bridge-controlled exciton–CT mixing. In contrast, in **Encap-TAT** a smaller LE–CT gap increases CT character and stabilises a CT-rich exciplex-like relaxed minimum, which competes with and suppresses iSF. For device applications, iSF scaffolds should therefore be engineered to maintain a sufficient LE–CT offset (avoiding excessive CT stabilisation) while keeping LE ↔ CT coupling in the moderate regime that supports CT-mediated super-exchange, alongside efficient pathways for triplet separation/harvesting. Overall, tuning the LE–CT energy gap and bridge–chromophore coupling strength provides a practical design lever to direct molecular assemblies toward either correlated triplet formation or exciplex-like relaxation and emission.

Author contributions

A. R. and H. B. conceived and supervised the project. E. S. carried out the experimental investigations, theoretical calculations and prepared the initial draft of the manuscript. J. W. performed the photoluminescence quantum yield (PLQY) measurements. D. G. C., J. R., S. M., O. M., and H. H. were involved in the synthesis and characterization of the materials. All authors contributed to the discussion of the results and to the final version of the manuscript. All authors except Chanakarn Phansa have given approval to the final version of the manuscript.

Conflicts of interest

All experimental/computational data and procedures are available in the SI.

Data availability

The data underlying all figures and tables in this article are publicly available from the University of Cambridge repository at https://doi.org/10.17863/CAM.129000. This repository includes the underlying datasets and the analysis outputs used to generate the figures. Any analysis code and scripts used for data processing, fitting, and figure generation are also available in the same repository. Additional supporting data are provided in the supplementary information (SI). Supplementary information: additional experimental details, characterization data, tables and figures. See DOI: https://doi.org/10.1039/d6sc00278a.

Acknowledgements

References

1 D. N. Congreve, J. Lee, N. J. Thompson, E. Hontz, S. R. Yost, P. D. Reusswig, M. E. Bahlke, S. Reineke, T. Van Voorhis and M. A. Baldo, *Science*, 2013, **340**, 334–337.

2 M. B. Smith and J. Michl, *Chem. Rev.*, 2010, **110**, 6891–6936.

3 A. Rao and R. H. Friend, *Nat. Rev. Mater.*, 2017, **2**, 1–12.

4 J. Xia, S. N. Sanders, W. Cheng, J. Z. Low, J. Liu, L. M. Campos, T. J. Sun Xia, W. Cheng, J. Liu, T. Sun, S. N. Sanders, J. Z. Low, L. M. Campos and J. Xia, *Adv. Mater.*, 2017, **29**, 1601652.

5 A. Kunzmann, M. Gruber, R. Casillas, J. Zirzlmeier, M. Stanzel, W. Peukert, R. R. Tykwinski and D. M. Guldi, *Angew. Chem., Int. Ed.*, 2018, **57**, 10742–10747.

6 O. V. Mikhnenko, P. W. M. Blom and T. Q. Nguyen, *Energy Environ. Sci.*, 2015, **8**, 1867–1888.

7 S. T. Roberts, R. E. McAnally, J. N. Mastron, D. H. Webber, M. T. Whited, R. L. Brutchey, M. E. Thompson and S. E. Bradforth, *J. Am. Chem. Soc.*, 2012, **134**, 6388–6400.

8 S. W. Eaton, L. E. Shoer, S. D. Karlen, S. M. Dyar, E. A. Margulies, B. S. Veldkamp, C. Ramanan, D. A. Hartzler, S. Savikhin, T. J. Marks and M. R. Wasielewski, *J. Am. Chem. Soc.*, 2013, **135**, 14701–14712.

9 B. S. Basel, J. Zirzlmeier, C. Hetzer, B. T. Phelan, M. D. Krzyaniak, S. R. Reddy, P. B. Coto, N. E. Horwitz, R. M. Young, F. J. White, F. Hampel, T. Clark, M. Thoss, R. R. Tykwinski, M. R. Wasielewski and D. M. Guldi, *Nat. Commun.*, 2017, **8**, 1–8.

10 S. N. Sanders, E. Kumarasamy, A. B. Pun, M. T. Trinh, B. Choi, J. Xia, E. J. Taffet, J. Z. Low, J. R. Miller, X. Roy, X. Y. Zhu, M. L. Steigerwald, M. Y. Sfeir and L. M. Campos, *J. Am. Chem. Soc.*, 2015, **137**, 8965–8972.

11 J. Kim, D. C. Bain, V. Ding, K. Majumder, D. Windemuller, J. Feng, J. Wu, S. Patil, J. Anthony, W. Kim and A. J. Musser, *Nat. Chem.*, 2024, **16**, 1680–1686.

12 K. C. Krishnapriya, P. Roy, B. Puttaraju, U. Salzner, A. J. Musser, M. Jain, J. Dasgupta and S. Patil, *Nat. Commun.*, 2019, **10**, 1–8.

13 G. He, E. M. Churchill, K. R. Parenti, J. Zhang, P. Narayanan, F. Namata, M. Malkoch, D. N. Congreve, A. Cacciuto, M. Y. Sfeir and L. M. Campos, *Nat. Commun.*, 2023, **14**, 1–10.

14 E. Busby, J. Xia, Q. Wu, J. Z. Low, R. Song, J. R. Miller, X. Y. Zhu, L. M. Campos and M. Y. Sfeir, *Nat. Mater.*, 2015, **14**, 426–433.

15 A. B. Pun, S. N. Sanders, E. Kumarasamy, M. Y. Sfeir, D. N. Congreve, L. M. Campos, A. B. Pun, S. N. Sanders, E. Kumarasamy, L. M. Campos, M. Y. Sfeir and D. N. Congreve, *Adv. Mater.*, 2017, **29**, 1701416.

16 T. Yamakado, S. Takahashi, K. Watanabe, Y. Matsumoto, A. Osuka, S. Saito, T. Yamakado, S. Takahashi, K. W. Atanabe, Y. M. Atsumoto, P. R. A. Osuka and S. Saito, *Angew. Chem., Int. Ed.*, 2018, **57**, 5438–5443.

17 L. Schaufelberger, J. T. Blaskovits, R. Laplaza, K. Jorner and C. Corminboeuf, *Angew. Chem., Int. Ed.*, 2025, **64**, e202415056.

18 S. Nakamura, H. Sakai, M. Fuki, R. Ooie, F. Ishiwari, A. Saeki, N. V. Tkachenko, Y. Kobori and T. Hasobe, *Angew. Chem., Int. Ed.*, 2023, **62**, e202217704.

19 A. M. Levine, G. He, G. Bu, P. Ramos, F. Wu, A. Soliman, J. Serrano, D. Pietraru, C. Chan, J. D. Batteas, M. Kowalczyk, S. J. Jang, B. L. Nannenga, M. Y. Sfeir, E. H. R. Tsai and A. B. Braunschweig, *J. Phys. Chem. C*, 2021, **125**, 12207–12213.

20 A. B. Pun, A. Asadpoordarvish, E. Kumarasamy, M. J. Y. Tayebjee, D. Niesner, D. R. McCamey, S. N. Sanders, L. M. Campos and M. Y. Sfeir, *Nat. Chem.*, 2019, **11**, 821–828.

21 Y. Hong, M. Rudolf, M. Kim, J. Kim, T. Schembri, A. M. Krause, K. Shoyama, D. Bialas, M. I. S. Röhr, T. Joo, H. Kim, D. Kim and F. Würthner, *Nat. Commun.*, 2022, (13), 1–11.

22 T. Ullrich, P. Pinter, J. Messelberger, P. Haines, R. Kaur, M. M. Hansmann, D. Munz and D. M. Guldi, *Angew. Chem.*, 2020, **132**, 7980–7988.

23 E. A. Margulies, Y. L. Wu, P. Gawel, S. A. Miller, L. E. Shoer, R. D. Schaller, F. Diederich and M. R. Wasielewski, *Angew. Chem., Int. Ed.*, 2015, **54**, 8679–8683.

24 C. Hetzer, D. M. Guldi and R. R. Tykwinski, *Chem.–Eur. J.*, 2018, **24**, 8245–8257.

25 B. S. Basel, R. M. Young, M. D. Krzyaniak, I. Papadopoulos, C. Hetzer, Y. Gao, N. T. La Porte, B. T. Phelan, T. Clark, R. R. Tykwinski, M. R. Wasielewski and D. M. Guldi, *Chem. Sci.*, 2019, **10**, 11130–11140.

26 E. A. Margulies, C. E. Miller, Y. Wu, L. Ma, G. C. Schatz, R. M. Young and M. R. Wasielewski, *Nat. Chem.*, 2016, **8**, 1120–1125.

27 M. J. Y. Tayebjee, S. N. Sanders, E. Kumarasamy, L. M. Campos, M. Y. Sfeir and D. R. McCamey, *Nat. Phys.*, 2017, **13**, 182–188.

28 K. R. Parenti, R. Chesler, G. He, P. Bhattacharyya, B. Xiao, H. Huang, D. Malinowski, J. Zhang, X. Yin, A. Shukla, S. Mazumdar, M. Y. Sfeir and L. M. Campos, *Nat. Chem.*, 2023, **15**, 339–346.

29 T. Wang, H. Liu, X. Wang, L. Tang, J. Zhou, X. Song, L. Lv, W. Chen, Y. Chen and X. Li, *J. Mater. Chem. A*, 2023, **11**, 8515–8539.

30 W. Kim and A. J. Musser, *Adv. Phys.:X*, 2021, **6**, 1918022.

31 W. B. Davis, W. A. Svec, M. A. Ratner and M. R. Wasielewski, *Nature*, 1998, **396**, 60–63.

32 K. Majumder, S. Mukherjee, J. Park, W. Kim, A. J. Musser and S. Patil, *Angew. Chem., Int. Ed.*, 2024, **63**, e202408615.

33 M. Majdecki, C. H. Hsu, C. H. Wang, E. H. C. Shi, M. Zakrocka, Y. C. Wei, B. H. Chen, C. H. Lu, S. Da Yang, P. T. Chou and P. Gaweł, *Angew. Chem., Int. Ed.*, 2024, **63**, e202401103.

34 E. Kumarasamy, S. N. Sanders, M. J. Y. Tayebjee, A. Asadpoordarvish, T. J. H. Hele, E. G. Fuemmeler, A. B. Pun, L. M. Yablon, J. Z. Low, D. W. Paley, J. C. Dean, B. Choi, G. D. Scholes, M. L. Steigerwald, N. Ananth,

35 T. Wang, S. Zhang, Y. T. Ding, B. Y. Zhang, B. Yu, R. Xu, Z. X. Liu, C. L. Sun, C. Zhang, Q. Wang and H. L. Zhang, *J. Mater. Chem. C*, 2025, **13**, 9576–9583.

36 T. C. Berkelbach, M. S. Hybertsen and D. R. Reichman, *J. Chem. Phys.*, 2013, **138**, 114103.

37 B. S. Basel, C. Hetzer, J. Zirzlmeier, D. Thiel, R. Guldi, F. Hampel, A. Kahnt, T. Clark, D. M. Guldi and R. R. Tykwinski, *Chem. Sci.*, 2019, **10**, 3854–3863.

38 L. C. Lin, T. Smith, Q. Ai, B. K. Rugg, C. Risko, J. E. Anthony, N. H. Damrauer and J. C. Johnson, *Chem. Sci.*, 2023, **14**, 11554–11565.

39 B. Carlotti, I. K. Madu, H. Kim, Z. Cai, H. Jiang, A. K. Muthike, L. Yu, P. M. Zimmerman and T. Goodson, *Chem. Sci.*, 2020, **11**, 8757–8770.

40 H. M. Bergman, G. R. Kiel, R. J. Witzke, D. P. Nenon, A. M. Schwartzberg, Y. Liu and T. D. Tilley, *J. Am. Chem. Soc.*, 2020, **142**, 19850–19855.

41 D. Bansal, A. Kundu, V. P. Singh, A. K. Pal, A. Datta, J. Dasgupta and P. Mukhopadhyay, *Chem. Sci.*, 2022, **13**, 11506–11512.

42 W. Ishii, M. Fuki, E. M. Bu Ali, S. Sato, B. Parmar, A. Yamauchi, C. H. Mulyadi, M. Uji, S. Medina Rivero, G. Watanabe, J. Clark, Y. Kobori and N. Yanai, *J. Am. Chem. Soc.*, 2024, **146**, 25527–25535.

43 A. Mohanty, V. P. Singh, C. M. Hussain, M. Dey, D. Ghosh, P. Mukhopadhyay and J. Dasgupta, *Chem. Sci.*, 2025, **16**, 21368–21378.

44 A. Neef, S. Beaulieu, S. Hammer, S. Dong, J. Maklar, T. Pincelli, R. P. Xian, M. Wolf, L. Rettig, J. Pflaum and R. Ernstorfer, *Nature*, 2023, **616**, 275–279.

45 H. Miyamoto, K. Okada, K. Tada, R. Kishi and Y. Kitagawa, *Molecules*, 2024, **29**, 5449.

46 Y. Bo, Y. Hou, D. A. X. Lavergne, T. Clark, M. J. Ferguson, R. R. Tykwinski and D. M. Guldi, *Nat. Commun.*, 2025, **16**, 1–12.

47 Y. J. Bae, D. Shimizu, J. D. Schultz, G. Kang, J. Zhou, G. C. Schatz, A. Osuka and M. R. Wasielewski, *J. Phys. Chem. A*, 2020, **124**, 8478–8487.

48 C. B. Dover, J. K. Gallaher, L. Frazer, P. C. Tapping, A. J. Petty, M. J. Crossley, J. E. Anthony, T. W. Kee and T. W. Schmidt, *Nat. Chem.*, 2018, **10**, 305–310.

49 X. Feng and A. I. Krylov, *Phys. Chem. Chem. Phys.*, 2016, **18**, 7751–7761.

50 S. Valianti and S. S. Skourtis, *J. Phys. Chem. Lett.*, 2022, **13**, 939–946.

51 K. R. Parenti, G. He, S. N. Sanders, A. B. Pun, E. Kumarasamy, M. Y. Sfeir and L. M. Campos, *J. Phys. Chem. A*, 2020, **124**, 9392–9399.

52 J. Royakkers, A. Minotto, D. G. Congrave, W. Zeng, A. Patel, A. D. Bond, D. K. Bučar, F. Cacialli and H. Bronstein, *J. Org. Chem.*, 2020, **85**, 207–214.

53 A. B. Pun, S. N. Sanders, M. Y. Sfeir, L. M. Campos and D. N. Congreve, *Chem. Sci.*, 2019, **10**, 3969–3975.

54 K. A. Kistler, C. M. Pochas, H. Yamagata, S. Matsika and F. C. Spano, *J. Phys. Chem. B*, 2012, **116**, 77–86.

55 F. Gao, Y. Zhao and W. Liang, *J. Phys. Chem. B*, 2011, **115**, 2699–2708.

56 N. J. Hestand and F. C. Spano, *Chem. Rev.*, 2018, **118**, 7069–7163.

57 T. J. H. Hele, E. G. Fuemmeler, S. N. Sanders, E. Kumarasamy, M. Y. Sfeir, L. M. Campos and N. Ananth, *J. Phys. Chem. A*, 2019, **123**, 2527–2536.

58 E. Sebastian and M. Hariharan, *J. Am. Chem. Soc.*, 2021, **143**, 13769–13781.

59 N. J. Hestand and F. C. Spano, *Acc. Chem. Res.*, 2017, **50**, 341–350.

60 N. J. Hestand and F. C. Spano, *J. Chem. Phys.*, 2015, **143**, 244707.

61 D. Bialas, C. Brüning, F. Schlosser, B. Fimmel, J. Thein, V. Engel and F. Würthner, *Chem.–Eur. J.*, 2016, **22**, 15011–15018.

62 P. Ottiger, H. Köppel and S. Leutwyler, *Chem. Sci.*, 2015, **6**, 6059–6068.

63 R. Jing, Y. Li, K. Tajima, Y. Wan, N. Fukui, H. Shinokubo, Z. Kuang and A. Xia, *J. Phys. Chem. Lett.*, 2024, **15**, 1469–1476.

64 E. Sebastian, J. Sunny and M. Hariharan, *Chem. Sci.*, 2022, **13**, 10824–10835.

65 R. M. Young and M. R. Wasielewski, *Acc. Chem. Res.*, 2020, **53**, 1957–1968.

66 J. Hoche, M. Flock, X. Miao, L. N. Philipp, M. Wenzel, I. Fischer and R. Mitric, *Chem. Sci.*, 2021, **12**, 11965–11975.

67 S. F. Völker, A. Schmiedel, M. Holzapfel, K. Renziehausen, V. Engel and C. Lambert, *J. Phys. Chem. C*, 2014, **118**, 17467–17482.

68 J. Seibt, P. Marquetand, V. Engel, Z. Chen, V. Dehm and F. Würthner, *Chem. Phys.*, 2006, **328**, 354–362.

69 E. Kirchner, D. Bialas and F. Würthner, *Chem.–Eur. J.*, 2019, **25**, 11294–11301.

70 J. J. Snellenburg, S. Laptenok, R. Seger, K. M. Mullen and I. H. M. van Stokkum, *J. Stat. Software*, 2012, **49**, 1–22.

71 I. H. M. Van Stokkum, D. S. Larsen and R. Van Grondelle, *Biochim. Biophys. Acta Bioenerg.*, 2004, **1657**, 82–104.

72 H. L. Stern, A. J. Musser, S. Gelinas, P. Parkinson, L. M. Herz, M. J. Bruzek, J. Anthony, R. H. Friend and B. J. Walker, *Proc. Natl. Acad. Sci. U. S. A.*, 2015, **112**, 7656–7661.

73 Z. Wang, H. Liu, X. Xie, C. Zhang, R. Wang, L. Chen, Y. Xu, H. Ma, W. Fang, Y. Yao, H. Sang, X. Wang, X. Li and M. Xiao, *Nat. Chem.*, 2021, **13**, 559–567.

74 Y. Bo, Y. Hou, D. Thiel, R. Weiß, T. Clark, M. J. Ferguson, R. R. Tykwinski and D. M. Guldi, *J. Am. Chem. Soc.*, 2023, **145**, 18260–18275.

75 O. Millington, S. Montanaro, A. Sharma, S. A. Dowland, J. Winkel, J. Grune, A. Leventis, T. Bennett, J. Shaikh, N. Greenham, A. Rao and H. Bronstein, *J. Am. Chem. Soc.*, 2024, **146**, 29664–29674.

76 V. Abraham and N. J. Mayhall, *J. Phys. Chem. Lett.*, 2021, **12**, 10505–10514.

77 R. A. Krueger and G. Blanquart, *J. Phys. Chem. A*, 2019, **123**, 1796–1806.

78 J. Choi, S. Kim, M. Ahn, J. Kim, D. W. Cho, D. Kim, S. Eom, D. Im, Y. Kim, S. H. Kim, K. R. Wee and H. Ihee, *Commun. Chem.*, 2023, **6**, 1–11.

79 N. J. Hestand, H. Yamagata, B. Xu, D. Sun, Y. Zhong, A. R. Harutyunyan, G. Chen, H. L. Dai, Y. Rao and F. C. Spano, *J. Phys. Chem. C*, 2015, **119**, 22137–22147.

80 H. Yamagata, J. Norton, E. Hontz, Y. Olivier, D. Beljonne, J. L. Brédas, R. J. Silbey and F. C. Spano, *J. Chem. Phys.*, 2011, **134**, 204703.

81 S. Lukman, K. Chen, J. M. Hodgkiss, D. H. P. Turban, N. D. M. Hine, S. Dong, J. Wu, N. C. Greenham and A. J. Musser, *Nat. Commun.*, 2016, (7), 1–13.

82 Y. Ishino, K. Miyata, T. Sugimoto, K. Watanabe, Y. Matsumoto, T. Uemura and J. Takeya, *Phys. Chem. Chem. Phys.*, 2014, **16**, 7501–7512.